

Estimating Important Electrode Parameters of High Temperature PEM Fuel Cells By Fitting a Model to Polarisation Curves and Impedance Spectra

Vang, Jakob Rabjerg; Zhou, Fan; Andreassen, Søren Juhl; Kær, Søren Knudsen

Published in:
ECS Transactions

DOI (link to publication from Publisher):
[10.1149/06803.0013ecst](https://doi.org/10.1149/06803.0013ecst)

Publication date:
2015

Document Version
Early version, also known as pre-print

[Link to publication from Aalborg University](#)

Citation for published version (APA):

Vang, J. R., Zhou, F., Andreassen, S. J., & Kær, S. K. (2015). Estimating Important Electrode Parameters of High Temperature PEM Fuel Cells By Fitting a Model to Polarisation Curves and Impedance Spectra. *ECS Transactions*, 68(3), 13-34 . <https://doi.org/10.1149/06803.0013ecst>

General rights

Copyright and moral rights for the publications made accessible in the public portal are retained by the authors and/or other copyright owners and it is a condition of accessing publications that users recognise and abide by the legal requirements associated with these rights.

- Users may download and print one copy of any publication from the public portal for the purpose of private study or research.
- You may not further distribute the material or use it for any profit-making activity or commercial gain
- You may freely distribute the URL identifying the publication in the public portal -

Take down policy

If you believe that this document breaches copyright please contact us at vbn@aub.aau.dk providing details, and we will remove access to the work immediately and investigate your claim.

Estimating Important Electrode Parameters of High Temperature PEM Fuel Cells by Fitting a Model to Polarisation Curves and Impedance Spectra

J. R. Vang^a, F. Zhou^a, S. J. Andreasen^{ab}, S. K. Kær^a

^a Department of Energy Technology, Aalborg University, 9220 Aalborg East, DK

^b Serenergy A/S, 9000 Aalborg, DK

A high temperature PEM (HTPEM) fuel cell model capable of simulating both steady state and dynamic operation is presented. The purpose is to enable extraction of unknown parameters from sets of impedance spectra and polarisation curves. The model is fitted to two polarisation curves and four impedance spectra measured on a Dapozol 77 MEA. The model is capable of achieving good agreement with the recorded curves. Except at OCV, where the voltage is overpredicted, the simulated polarisation curves deviate maximum 3.0% from the measurements. The impedance spectra deviate maximum 3.7%. The fitted parameter values are within the range reported in literature. The only exception is the catalyst layer acid content, which is an order of magnitude lower. This may derive from acid migration. The model is used to illustrate the effect of reactant dynamics on the impedance spectrum. The model can aid in the analysis of data from degradation tests.

Nomenclature

Variable [unit]	Description	Variable [unit]	Description
a_i	Activity of reactant i	RH	Relative humidity
$A_{C,m}$ [$\text{m}^2 \text{kg}^{-1}$]	Carbon surface area	S_i [$\text{mol m}^{-3} \text{s}^{-1}$]	Source term of species i
$A_{Pt,V}$ [$\text{m}_{Pt}^2 \text{m}^{-3}$]	ECSA per CL volume	T [K]	Absolute temperature
A_{surf} [$\text{m}^2 \text{m}^{-2}$]	CL pore surface area	T_c [$^{\circ}\text{C}$]	Celsius temperature
c [mol m^{-3}]	Total molar concentration	t_j [m]	Thickness of MEA layer j
c_i [mol m^{-3}]	Molar concentration of i	\mathbf{u} [m s^{-1}]	Velocity vector
$c_{O_2,i}$ [$\text{mol m}^{-3} \text{atm}^{-1}$]	Oxygen solubility in phase i	V [V]	Cell voltage
C_{dl} [F m^{-2}]	Double layer capacitance	V_{PA} [$\text{m}^3 \text{m}^{-2}$]	Area specific acid volume.
d_{film} [m]	Acid film thickness	V_{pore} [$\text{m}^3 \text{m}^{-2}$]	Specific pore volume.
D_i [$\text{m}^2 \text{s}^{-1}$]	Diffusion coefficient of i	$w_{H_3PO_4}$	H_3PO_4 mass fraction
D_{ij} [$\text{m}^2 \text{s}^{-1}$]	Binary diffusion coefficient	X	H_3PO_4 per PBI repeat unit
E [V]	Open circuit potential	y_i	Mole fraction
F [C mol^{-1}]	Faraday's constant	ΔS_0 [J $\text{mol}^{-1} \text{K}^{-1}$]	Reaction entropy
i [A cm^{-2}]	Cell level current density	ϵ	Porosity
i_{Pt} [A m_{Pt}^{-2}]	Current density per ECSA	$\epsilon_{i(j)}$	Volume fraction of i (in j)
i_0 [A m_{Pt}^{-2}]	Exchange current density	H [V]	Overpotential
j_V [A m^{-3}]	Volumetric current density	κ_i [S m^{-1}]	Ionic conductivity
k_p [m^2]	Permeability	M [$\text{kg m}^{-1} \text{s}^{-1}$]	Dynamic viscosity
L_i [kg m^{-2}]	Loading of i in CL	P [kg m^{-3}]	Density
M [kg mol^{-1}]	Molar mass	ϕ_e [V]	Electronic potential
R_{cell} [Ωcm^2]	Cell contact resistance	ϕ_i [V]	Ionic potential

Introduction

The use of high temperature PEM (HTPEM) fuel cells based on phosphoric acid (PA) doped PBI membranes for efficient conversion of various fuels to electrical energy has promising prospects for a number of reasons. One important aspect is the tolerance to fuel impurities. HTPEM fuel cells can run on reformed hydrocarbon or alcohol fuels without the complicated gas cleaning procedures that are needed when using reformat in low temperature PEM (LTPEM) fuel cells. The CO tolerance of HTPEM fuel cells is in the order of % (1,2), while it is on the order of tens of ppm for LTPEM fuel cells (3,4). The high operating temperature (120 °C - 180 °C) also both enables efficient cooling of the fuel cells and yields high quality waste heat. The combination of good impurity tolerance and high quality waste heat makes HTPEM fuel cells well suited for combined heat and power applications and for integration with simple reformer systems. PA also has the advantageous property of retaining some conductivity even at very low humidity. This means that HTPEM fuel cells can operate without humidification as opposed to LTPEM fuel cells. This again means that HTPEM systems can be made simpler, compared to LTPEM systems. The advantages of HTPEM fuel cells come at a price, however. PA tends to adsorb on the platinum catalyst and thus the available electrochemical surface area (ECSA) is reduced in comparison with LTPEM fuel cells. Also, the conductivity of PA-PBI membranes is generally lower than for Nafion membranes (5). In order to improve the performance of HTPEM fuel cells it is necessary to increase the understanding of the processes occurring within the cell during operation.

One way to achieve insight into the nature of fuel cell processes is to model them mathematically. The advantage of modelling is the possibility to investigate many different cases which would be too time-consuming to investigate experimentally. Also, models have the power to estimate variables which cannot be measured in an actual operating fuel cell. One of the many challenges in modelling of fuel cells is the large number of variables, which affect the performance of the cell. When using the traditional approach of modelling the fuel cell in steady state only and comparing the results to steady state polarisation curves, a problem arises. Unless the available information about the fuel cell is complete, the number of fitting variables quickly becomes prohibitively large, and the number of variable combinations, which give acceptable fits, also become large. This will especially be true for a model of some complexity. A way to decrease the number of degrees of freedom, and thus increase the likelihood of arriving at a physically sensible fit, is to include data from another characterisation method in the fit. One possible candidate for this task is electrochemical impedance spectroscopy (EIS). In EIS, the impedance of the fuel cell is determined by superimposing a sinusoidal signal on the current or voltage of the fuel cell, measuring the response and calculating the impedance from the phase shift and the signal amplitude ratios. The impedance spectrum is recorded by performing this operation at a number of frequencies of the impedance signal. By developing a model which can simulate both the dynamic and the steady state performance, both impedance spectra and polarisation curves can be taken into account when fitting. This will reduce the ambiguity of the fit, since parameter combinations that produce similar polarisation curves may produce vastly different impedance spectra and vice versa.

Quite a number of HTPEM fuel cell models exist in the literature. These range from simple lumped models (6) over 1D (7) and 2D (8) models to full 3D CFD models (9–11). When fitting models to fuel cell impedance spectra, the models used are typically simple equivalent circuit models (12–14). While these models can be useful for quantifying changes to the impedance spectrum as operating parameters are changed or the fuel cell degrades, the mechanistic insights provided by these models are limited by their empirical nature. Some models take physics into account by using simplified linearised versions of the most important transport equations to derive the fuel cell impedance as a function of perturbation frequency. Most of these models concern themselves with low temperature PEM (LTPEM) fuel cells. One example of an LTPEM impedance model compared the effects of different reaction mechanisms (15). Combined modelling of steady state performance and impedance has only been performed a few times. One such model was a 1+1D model of an LTPEM fuel cell focusing on the gas channel dynamics (16). The model results were not directly compared to experimental data. Another example is the work by Roy et al. (17), where a steady state and a frequency dependent model were developed to investigate the effects of reaction mechanisms on the low frequency loop in the impedance spectrum. One model concerning HTPEM fuel cells was presented by Boaventura et al. (18) They constructed a simple 1D dynamic model considering the dynamics of gas transport and double layer charging. The model was capable of fitting the polarisation data quite well, but fell short in matching the time scales in the impedance spectra. Recently, an HTPEM impedance model was developed by Shamardina et. al. (19) Apart from impedance, the model was able to simulate polarisation curves, step changes in potential and current interrupt. The model was capable of extracting electrode parameters to fit a polarisation curve from one impedance spectrum for a cell of around 1 cm². Another study dealt with impedance and steady state behaviour of solid oxide fuel cells (20). The model used was a dynamic 2D along-the-channel type, which took into account mass transport and heat transfer. The model was validated against button cell data, showing good agreement when heat transfer and momentum was neglected. No validation was performed with respect to full size cells. Simulations using the full model showed significant effects of convection and temperature on the impedance spectrum. Recently, Baricci et al.(21) presented a quasi 2D HTPEM model capable of simulating both impedance spectra and polarisation curves. The model utilised a combination of analytical and numerical solution of the governing equations in order to decrease computational time. Very good agreement was obtained when fitting the model to experimental data in the current density range of 0.05 – 0.4 A cm⁻². The effect of changing stoichiometry was also reproduced at one current density. The fitted cell parameters were compared to literature data and the agreement was generally good. This author group previously attempted to develop a 2D transient fuel cell model to simulate impedance spectra and polarisation curves for an HTPEM fuel cell (22). The model turned out to be too simplistic in some respects, since it was not possible to achieve a good fit to the polarisation curve and the impedance spectrum simultaneously.

Experimental

In order to get sets of impedance spectra and polarisation curves for fitting and validating the model, a series of measurements on HTPEM fuel cells have been performed in the laboratory. Measurements were carried out in a G60 single cell test

bench from Greenlight Innovation. The MEA used was a Dapozol 77 from Danish Power Systems (DPS). Impedance was recorded using a Gamry Reference 3000 impedance analyser.

The Setup

The setup consisted of a custom made single cell assembly where the 46 cm² MEA was sandwiched between two carbon composite flow plates with serpentine flow fields. The anode side had two parallel channels and the cathode side had three. Teflon gaskets with a thickness of 250 μ m were used to make the assembly gas tight. The load module was connected by two brass current collector plates. The cell was held together by two steel end plates which also served as manifolds for the reactant supply. The end plates were clamped using eight screws which were tightened using a torque of 0.3 Nm. Reactants were supplied by mass flow controllers. The setup is capable of running on mixtures of H₂, CO₂, CO, and MeOH but only pure hydrogen was used for the present study. The reactants were humidified at room temperature prior to feeding to the fuel cell. Setup operation was controlled by a build in PC with a Labview based interface. A schematic drawing of the setup is shown in Figure 1.

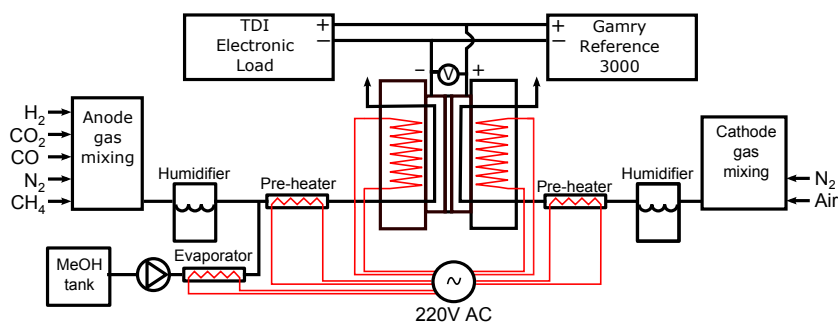


Figure 1. A schematic drawing of the experimental setup.

Measurement Procedure

The recording of impedance and polarisation data was performed through an automation script which enables generation of large amounts of data with minimal manual effort. The fuel cell was first run at the lowest temperature of interest. The system waited until steady state had been achieved and then recorded a polarisation curve by sampling at uniformly spaced current points from 0 to 50 A. Subsequently, impedance spectra were recorded at different currents. At each current, the system waited until steady state was achieved before measuring. Two spectra were recorded at each point to assess repeatability. The impedance was recorded from 10 kHz to 0.1 Hz. Data was recorded at the temperatures of 140 °C – 180 °C, air stoichiometry of 2 and 4, H₂ stoichiometry of 1.2, and EIS currents of 5-20 A.

Modelling

In this section, the mathematical framework for the fuel cell model is presented. The fuel cell model is developed using the Matlab software package. The model

takes into account species transport, electrode kinetics, potential distribution and effects of phosphoric acid water content on the electrochemical processes.

Assumptions and simplifications

The following simplifying assumptions have been made in the development of the model:

1. All species are assumed to obey the ideal gas law.
2. The temperature is assumed constant throughout the fuel cell.
3. The anode processes are disregarded in the calculations.
4. The feed air consists only of N_2 , O_2 , and H_2O . Dry air is assumed to be 21% O_2 and 79% N_2 .
5. The flow in the gas channel is assumed to be inviscid.
6. The gas diffusion layer and the catalyst layer are assumed to be macro-homogeneous.
7. The micro-porous layer on the GDL is neglected in the model. The effects are lumped with those of the GDL.
8. The phosphoric acid and the gas phase are assumed to be in equilibrium with respect to water content.

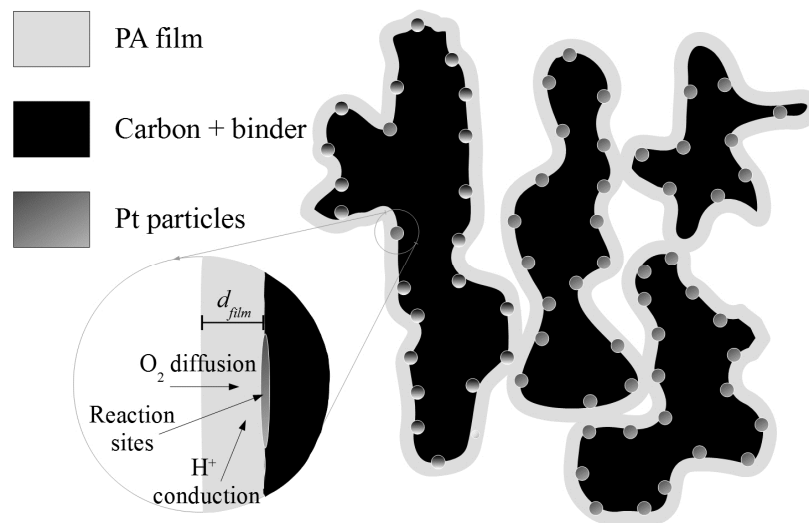


Figure 2: Schematic of the thin film catalyst layer model.

Figure 2 shows an illustration of the catalyst layer model. The catalyst particles are assumed to be dispersed uniformly on the surface of the catalyst layer solid phase. The catalyst layer phosphoric acid is assumed evenly distributed over the entire surface of the solid phase. An illustration of the computational domain is given in Figure 3. The fuel cell is resolved in 1D through the membrane (x-direction). The channel is resolved separately along the length (y-direction) in order to better account for the effect on the fuel cell dynamics.

The computational domain is discretised in order to enable solution of the governing equations. The most important processes occur in the CL and thus this area has more cells than the other domains in spite of the relatively low volume of

the CL. The CL has 35 cells, the GDL has 15 cells and the channel has 20 cells. The numbers are chosen as a compromise between computational speed and grid independence.

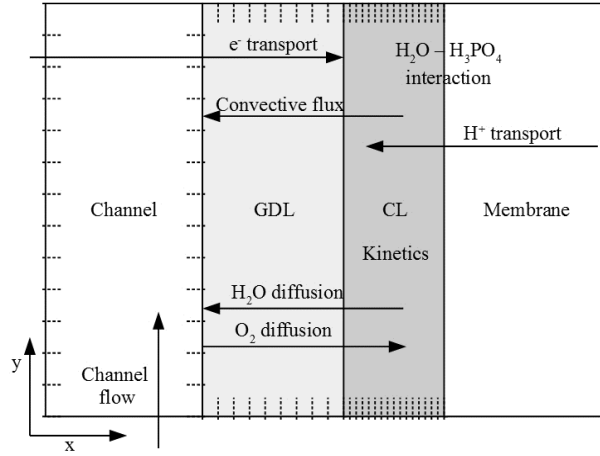


Figure 3: Schematic representation of the computational domain.

In order to represent the flow field dynamics as accurately as possible without resolving the model across the channel, some simplifications of the flow field geometry have been implemented. Instead of three serpentine channels separated by a land area, the fuel cell is assumed to have one straight channel of cross sectional area equal to that of the three channels and width equal to the width of the channels plus the land. This will introduce some inaccuracy due to the negligence of the land effects, but this simplification is necessary since resolving the cell in 2D will greatly increase solution times.

Governing equations

This section lists the differential equations which are solved when simulating the fuel cell operation. The model is developed on molar basis.

Species transport. In the transport of species, diffusion, convection and generation are taken into account. Oxygen and water are accounted for in this way. The conservation of nitrogen is taken care of by continuity.

$$\frac{\partial c y_i}{\partial t} = \frac{-\nabla(\mathbf{u} c y_i) + \nabla(c D_i \nabla y_i) + S_i}{\epsilon} \quad [1]$$

Here D_i and y_i are the diffusion coefficient and mole fraction of species i in the mixture, respectively, c is total molar concentration, ϵ is the porosity, \mathbf{u} is the velocity vector, and S_i is the source term accounting for generation or consumption of species i . This term is zero outside the catalyst layer. For oxygen, the source term is:

$$S_{O_2} = \frac{j_V}{4F} \quad [2]$$

Here F is Faraday's constant and $j_V = A_{Pt,V} \cdot i_{Pt}$ is the current density per catalyst layer volume. i_{Pt} is the local current density per platinum area, and $A_{Pt,V}$ is the catalyst surface area per CL volume. The water source term (S_{H_2O}) is more complex. Since PA exchanges water with the gas phase, the change in gas phase water content is dampened by the PA water content. The source term thus becomes:

$$\begin{aligned} S_{H_2O} &= -\frac{j_V}{2F} + \frac{\partial(c_{H_2O,tot})}{\partial t} \left(\frac{\partial c y_{H_2O}}{\partial c_{H_2O,tot}} - 1 \right) \\ &= \left(\nabla(\mathbf{u} c y_{H_2O}) + \nabla(c D_{H_2O} \nabla y_{H_2O}) + \frac{j_V}{2F} \right) \left(\frac{\partial c y_{H_2O}}{\partial c_{H_2O,tot}} - 1 \right) \end{aligned} \quad [3]$$

Continuity. The continuity equation is given as:

$$\frac{\partial c}{\partial t} = -\nabla(\mathbf{u} c) + S_{O_2} + S_{H_2O} \quad [4]$$

Overpotential. The cathode activation overpotential is governed by equation [5]. Here η is the activation overpotential, $\kappa_{i,CL}$ is the CL ionic conductivity, ϕ_i is the membrane phase potential, and C_{dl} is the cell area specific double layer capacitance and t_{CL} is the CL thickness.

$$\frac{\partial \eta}{\partial t} = \frac{-\nabla(\kappa_{i,CL} \nabla \phi_i) - j_V}{C_{dl}/t_{CL}} \quad [5]$$

Momentum transport. The momentum in the CL and GDL transport is assumed to be governed by Darcy's law. Since the flow velocities are low, the momentum dynamics have negligible effect on the overall system. Thus, they are assumed to be in quasi steady state and are solved explicitly for the velocity. Here k_p is the permeability and μ is the viscosity:

$$\mathbf{u} = \frac{k_p}{\mu} \nabla p \quad [6]$$

Channel dynamics. The channel model is simplified compared to the porous media model. The flow is assumed to be inviscid, so the continuity equation becomes $\nabla \mathbf{u} = 0$. Species transport is handled in the same way as in the porous media, except that diffusion in the y-direction is neglected due to the high flow rates. The only transport considered in the x-directions is the flux across the interface between the GDL and the channel. Inside the channel, species are assumed to mix perfectly in the x-direction. This gives:

$$\frac{\partial c y_i}{\partial t} = -\nabla(\mathbf{u} c y_i) + \frac{\partial(c D_i \partial y_i / \partial x)}{\partial x} \quad [7]$$

Constitutive relations

The way the model handles the quasi steady dependence of the variables is the area into which the most of the development work has been invested. The relations

presented in this section are used to determine the properties of the phosphoric acid in the CL, the reaction kinetics, and diffusion coefficients.

Phosphoric acid concentration. An attempt has been made to include all relevant dependencies on the concentration of the phosphoric acid inside the catalyst layer. An empirical relation for the concentration of the PA as a function of the gas phase relative humidity (RH) and absolute temperature (T) has been developed from the data presented by MacDonald and Boyack (23). The relation is given as:

$$w_{H_3PO_4} = w_1 + w_2 T + w_3 \ln(w_4 RH) + w_5 RH \quad [8]$$

Here $w_{H_3PO_4}$ is the H_3PO_4 mass fraction. The fitting constants are given in TABLE VII. For developing some relations, $w_{H_3PO_4}$ is converted to P_2O_5 mole fraction ($y_{P_2O_5}$) as in equation [9].

$$y_{P_2O_5} = \frac{0.724 w_{H_3PO_4} / M_{P_2O_5}}{0.724 w_{H_3PO_4} / M_{P_2O_5} + (1 - 0.724 w_{H_3PO_4}) / M_{H_2O}} \quad [9]$$

Solubility and diffusivity of O_2 in PA. Two important parameters, which depend on the PA concentration, are the solubility and diffusivity of O_2 in the acid film. Empirical relations for the solubility ($c_{0,O_2,PA}$) and the diffusivity ($D_{O_2,PA}$) of O_2 in PA have been developed using the data of Klinedinst et al. (24) and Gubbins and Walker (25) as well as the relation for solubility of O_2 in water developed by Tromans (26). For the solubility, it is assumed that the solubility of O_2 in aqueous PA is related to the solubility of O_2 in water ($c_{0,O_2,water}$) as in equation [10]. The equations for calculating $c_{0,O_2,water}$ are given in equation [28] in the appendix. Fitting coefficients c_{1-3} are given in TABLE VIII in the appendix.

$$c_{0,O_2,PA} = \frac{c_{0,O_2,water} \cdot c_1^{y_{P_2O_5}}}{c_2 (1 + y_{P_2O_5})^2} + c_3 \cdot y_{P_2O_5} \quad [10]$$

The diffusion coefficient is calculated in equation [11], using a relation suggested by Magalhaes et al. (27). The original relation uses absolute temperature, but here the Celsius scale (T_C) is used, since this improves the fit. The PA viscosity (μ_{PA}) is calculated using equation [29] given in the appendix.

$$D_{O_2,PA} = \exp \left(d_1 \cdot \ln \frac{T_C}{\mu_{PA}} + d_2 \right) \quad [11]$$

The relations for diffusivity and solubility are fitted simultaneously to the solubility data from Gubbins and Walker (25) and the diffusivity data and the diffusivity-solubility product data from Klinedinst et al. (24). The fitted coefficients are given in TABLE VIII in the appendix.

Proton conductivity. Proton conduction in the fuel cell is assumed to occur only in the PA phase. The conductivity of free PA ($\kappa_{i,PA}$) varies with PA concentration. Please refer to equations 3A and 3B in the work of MacDonald and Boyack (23) for the relation used in this work. Within the CL, the Bruggeman correction is applied in

order to correct for tortuosity and porosity as $\kappa_{i,CL} = \kappa_{i,PA} \cdot \epsilon_{PA}^{1.5}$. Here ϵ_{PA} is the volume fraction of PA in the CL. The conductivity of the membrane ($\kappa_{i,mem}$) is calculated by equation [12]. The expression is a regression to the conductivity data of Ma (28), measured at different PA doping levels, temperatures, and relative humidities. Ma only tested MEAs up to a doping level (X) of 7.2 H₃PO₄ per PBI repeat unit. The regression is used for extrapolation, since the MEA tested in this work has a membrane doping level of 10. The PA properties inside the membrane are assumed to be the same as on the interface between the cathode CL and the membrane.

$$\kappa_{i,mem} = 0.02845 \kappa_{i,PA}^{1.732} \cdot \epsilon_{PA,PBI}^{4.563} \quad [12]$$

The membrane volume fraction of PA ($\epsilon_{PA,PBI}$) is calculated as in equation [13]. The density of PBI is assumed to be $\rho_{PBI} = 1300 \text{ kg m}^{-3}$. The molar masses are $M_{H_3PO_4} = 0.098 \text{ kg mol}^{-1}$ and $M_{PBI} = 0.308 \text{ kg mol}^{-1}$. (10). The density of the acid (ρ_{PA}) is calculated using equation 1 in the work of MacDonald and Boyack (23).

$$\epsilon_{PA,PBI} = \frac{X \cdot M_{H_3PO_4} / (\rho_{PA} \cdot w_{H_3PO_4})}{X \cdot M_{H_3PO_4} / (\rho_{PA} \cdot w_{H_3PO_4}) + M_{PBI} / \rho_{PBI}} \quad [13]$$

The membrane thickness influences the resistive losses in the membrane. It is assumed to vary with the density of the acid in the membrane. The thickness is calculated as in equation [14]. The reference PA density $\rho_{PA,ref} = 1690 \text{ kg m}^{-3}$ is the density at the reference H₃PO₄ weight fraction $w_{H_3PO_4,ref} = 0.85$ at 25 °C.

$$t_{mem} = t_{mem,ref} \frac{X \cdot M_{H_3PO_4} / (\rho_{PA} \cdot w_{H_3PO_4}) + M_{PBI} / \rho_{PBI}}{X \cdot M_{H_3PO_4} / (\rho_{PA,ref} \cdot w_{H_3PO_4,ref}) + M_{PBI} / \rho_{PBI}} \quad [14]$$

Reaction kinetics. The reaction kinetics are modelled using the Butler-Volmer equation in equation [15]. Here i_{Pt} and i_0 are the current density and exchange current density per platinum surface area, respectively. $a_{O_2} = c_{O_2,Pt} / c_{O_2,ref}$ is the oxygen activity at the catalyst. c_{O_2} denotes oxygen concentration in the acid. Subscript *ref* denotes the reference value as opposed to the actual value at the catalyst (subscript Pt). The reference concentration is the equilibrium concentration in PA at 1 atm oxygen partial pressure. The water activity a_{H_2O} is calculated as the H₂O partial pressure over the standard atmospheric pressure. α is the transfer coefficient and η is the overpotential.

$$i_{Pt} = i_0 \left(a_{H_2O}^2 \cdot \exp\left(\frac{\alpha F}{RT} \eta\right) - a_{O_2} \cdot \exp\left(\frac{-\alpha F}{RT} \eta\right) \right) \quad [15]$$

The exchange current density depends on temperature and acid concentration as given in the empirical expression of equation [16]. The expression is fitted to the exchange current density data of Kunz and Gruver (29) after correcting the data using the OCV calculated at unit activity.

$$i_0 = \exp\left(\frac{-6450}{T} + 7.280\right) \quad [16]$$

The exchange current density is derived using $\alpha=1$. When $\alpha \neq 1$, i_0 will have to be corrected to avoid unreasonable ECSA values. Since α controls the Tafel slope, the correction consists of changing the current at which the curves with different α intersect. The intersection is assumed to take place at a superficial current density of 0.2 A cm^{-2} . The transition from the activation region to the ohmic region seems to take place around this point for the tested Dapozol[®] 77 MEA.

The oxygen concentration at the catalyst sites ($c_{\text{O}_2, \text{Pt}}$) is calculated using equation [17]. Here $c_{\text{O}_2, \text{PA}}$ is the equilibrium concentration of O_2 in phosphoric acid at the local conditions. The interface between the gas phase and the acid phase is assumed to be in equilibrium. $D_{\text{O}_2, \text{PA}}$ is the diffusion coefficient of oxygen in the acid film, and d_{film} is the acid film thickness.

$$c_{\text{O}_2, \text{Pt}} = c_{\text{O}_2, \text{PA}} + \frac{i_{\text{Pt}}}{4F} \cdot \frac{d_{\text{film}}}{D_{\text{O}_2, \text{PA}}} \quad [17]$$

The thickness of the PA film in the CL can be calculated, assuming that the carbon surface/volume ratio is determined by the carbon backing surface area. Here V_{PA} is the volume of PA per cell area, $A_{\text{C}, m}$ is the specific surface area of the carbon phase, $L_{\text{H}_3\text{PO}_4}$ and L_{C} are the loadings of pure H_3PO_4 and carbon per cell area, respectively. The binder is assumed not to affect the surface area.

$$d_{\text{film}} = \frac{V_{\text{PA}}}{A_{\text{C}, m} \cdot L_{\text{C}}} = \frac{L_{\text{H}_3\text{PO}_4} / (\rho_{\text{PA}} \cdot w_{\text{H}_3\text{PO}_4})}{A_{\text{C}, m} \cdot L_{\text{C}}} \quad [18]$$

Potential. The potentials considered in the model are the open circuit potential E , the electronic potential ϕ_e , the ionic potential ϕ_i , and the cathode overpotential η . Within the catalyst layer, these potentials are related as:

$$0 = \phi_e - \phi_i - \eta - E \quad [19]$$

E is calculated using the Nernst equation at unit activity with reference point 160°C ($T_0=433 \text{ K}$, $\Delta S_0 = -48.1 \text{ J mol}^{-1} \text{ K}^{-1}$, and $E_0 = 1.152 \text{ V}$).

$$E = E_0 + \Delta S_0 \cdot \frac{T - T_0}{2F} \quad [20]$$

The electronic potential is assumed constant across the CL. The value is determined from the cell voltage (V), the cell level current density (i), and the resistance of the cell assembly (R_{cell}), which is tuned by the fitting algorithm.

$$\phi_e = V + R_{\text{cell}} i \quad [21]$$

Gas phase diffusivities. When determining the diffusivity in the porous media, two phenomena are taken into account. These include continuum multi component diffusion, considering interaction of the diffusing species, and Knudsen diffusion, considering interactions with the pore walls. Knudsen diffusion is only considered in the CL, since the GDL pores are assumed too large for wall interactions to be

significant. The mixture diffusivity of species i is calculated from the binary diffusivities of i with respect to the other species j .

$$D_{i,mix} = \frac{1 - y_i}{\sum_j y_j / D_{ij}} \quad [22]$$

The binary diffusivities (D_{ij}) are corrected for temperature and pressure using equation [23]. γ is a species specific exponent. The reference values ($D_{ij,0}$) and exponents are given in TABLE IX in the appendix.

$$D_{ij} = D_{ij,0} \cdot \frac{P_0}{P} \left(\frac{T}{T_0} \right)^\gamma \quad [23]$$

The Knudsen diffusivity of species i ($D_{i,K}$) is calculated using the formulation given in Bird et al. (30). Here r [m] is the mean pore radius. The pore radius is estimated by assuming that the catalyst layer consists of identical cylindrical pores. The radius is then given by the ratio of the area specific void volume (V_{pore}) over the total CL wall surface area (A_{surf}).

$$D_{i,K} = \frac{8}{3} r \sqrt{\frac{RT}{2\pi M_i}} = \frac{8}{3} \frac{2V_{pore}}{A_{surf}} \sqrt{\frac{RT}{2\pi M_i}} = \frac{16}{3} \frac{t_{CL}\epsilon}{A_{C,m} \cdot L_C} \sqrt{\frac{RT}{2\pi M_i}} \quad [24]$$

The bulk diffusion coefficient is calculated by taking the inverse of the sum of diffusion resistances.

$$D_{i,bulk} = \frac{1}{1/D_{i,K} + 1/D_{i,mix}} \quad [25]$$

For the GDL, $D_{i,bulk} = D_{i,mix}$ since Knudsen diffusion is assumed to be unimportant here. The bulk diffusivity is corrected for porosity and tortuosity. In the CL, the Bruggeman correction is used: $D_{i,CL} = D_{i,bulk}\epsilon^{1.5}$. In the GDL, the relation of equation [26] given by Zamel et al. (31) is used.

$$D_{i,GDL} = 1.01(\epsilon - 0.24)^{1.83} D_{i,bulk} \quad [26]$$

Gas viscosity. The gas mixture viscosity is calculated using the Wilke relation as formulated in Bird et al. (30), page 27. The viscosities of the pure species are calculated using linear curve fits to tabulated data from the Engineering Equation Solver (EES) software package.

Summary. In this section, the mathematical framework for the mechanistic impedance model has been outlined. By solving the model in steady state and dynamic mode, steady state polarisation curves and impedance spectra can be simulated.

Model parameters

The parameters used when running the model can be divided into two categories. The fixed parameters are those which can be established from data sheets, the MEA manufacturer, or from the literature. The fitting parameters are the ones that are either completely unknown or where the uncertainty is deemed sufficiently large to have an important impact on the result. The model is fitted to impedance spectra and polarisation curves from a Dapozol 77 MEA. Most of the relevant data for the Dapozol MEAs has been supplied by the manufacturer. The known and assumed parameter values of the Dapozol 77 are given in TABLE I. The gas diffusion layer used is a Freudenberg H2315 C2. The relevant GDL data is extracted from the GDL data sheet (33). The fitting parameters are given in TABLE II.

TABLE I. Fixed fuel cell parameters

Parameter	Symbol	Value	Comment
GDL thickness	t_{GDL}	260 μm	Measured on GDL
GDL porosity	ϵ_{GDL}	0.78	Determined experimentally.
Reference Membrane thickness	$t_{mem,ref}$	80 μm	At room temperature, 85% H_3PO_4 acid. Value supplied by DPS.
Permeability	k_p	10^{-14} m^2	Converted from Air Resistance (Gurley) according to ISO 5636-5:2013(E) (32). Assumed equal for GDL and CL. (33)
Pt Loading	L_{Pt}	1.6 mg cm^{-2}	Value supplied by DPS.
Pt/C ratio in CL	$r_{Pt/C}$	0.6	Value supplied by DPS.
PBI/C ratio in CL	$r_{PBI/C}$	-	Proprietary information. Value supplied by DPS.
Cell area	A_{FC}	46 cm^2	Value supplied by DPS.
Channel width	W_{CH}	1.2 mm	Measured on the cathode flow plate.
Channel height	H_{CH}	1 mm	Measured on the cathode flow plate.
Land width	W_L	1.2 mm	Measured on the cathode flow plate.
Humidifier temperature	T_{humid}	27 $^{\circ}\text{C}$	Measured during data acquisition.

TABLE II. Fitting parameters

Parameter	Symbol	Comment
Catalyst ECSA	$A_{Pt,m}$	Controls exchange current density
Transfer coefficient	α	Controls Tafel slope
Carbon surface area	$A_{C,m}$	Controls PA film thickness and Knudsen diffusion coefficient
CL PA Loading	$L_{\text{H}_3\text{PO}_4}$	Controls CL conductivity and PA film thickness.
Double layer capacitance	C_{dl}	Controls dynamic behaviour of the cell.
CL thickness	t_{CL}	Approximately 25 μm according to DPS.
Cell contact resistance	R_{cell}	Accounts for the resistance of non-membrane components.

Results and discussion

The model described in the previous section is fitted to a set of polarisation curves and impedance spectra. The data used was recorded at 160 $^{\circ}\text{C}$ and air stoichiometry of 2 and 4. Impedance spectra recorded at 0.11 A cm^{-2} and 0.43 A cm^{-2}

are used. Fitting the model across more curves reduces the number of degrees of freedom. Figure 4 shows the fit to the impedance spectra. The agreement between the curves is generally good. The maximum deviation between the data and the fit is 3.8% of the maximum modulus. The maximum RMS deviation is 2.2%. The largest discrepancy is in the low frequency region between 1 Hz and 0.1 Hz. Here the model tends to under predict the impedance. In the region between 100 Hz and 10 Hz, the difference in the real part between the curves recorded at 0.11 A cm⁻² is underpredicted. This can be seen in greater detail in the right plot. It seems to be a result of the difference in resistance between the operating points not being properly reproduced by the model.

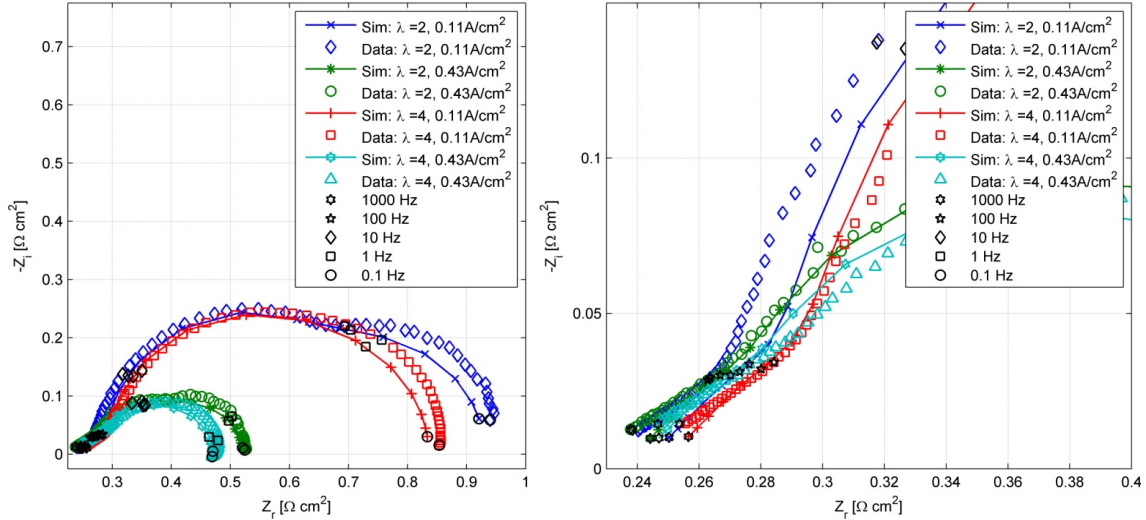


Figure 4. Left: Fit of the model to impedance spectra at different air stoichiometries and impedance currents. Right: Zoom of the high frequency region of the simulated and measured impedance spectra.

The fit to the polarisation curves is shown in Figure 5. The data and the simulations are in close agreement, except close to OCV, where the simulated voltage is overpredicted by 25%. In the rest of the range, the deviation is maximum of 3.0% of the maximum voltage. In most of the current range, the voltage is slightly underpredicted, since the slopes of the simulated curves are steeper than those of the measured curves. The simulated curves also differ from the data by having no discernible mass transport limited region. The discrepancy at low current is at least partly due to the model not considering reactant cross-over. This can be rationalised by adding a crude hydrogen cross-over model. This model assumes that the diffusivity of hydrogen in the membrane can be approximated by $D_{H_2,mem} = 2D_{O_2,PA}$ and the solubility is $c_{H_2,mem} = 4c_{O_2,PA}$. The anode side hydrogen partial pressure is assumed to be 0.9 atm and the crossing hydrogen is assumed to be instantly oxidised when reaching the cathode. If Δx is the step size in the CL, then the volumetric current density in the cell closest to the membrane is given by equation [27]. The effect on the polarisation curve can be seen in Figure 5. The effects on the impedance spectra are negligible and thus not shown. While the observed effect indicates that cross-over plays a role in the low OCV of HTPEM fuel cells, a proper model, taking into account transient variations of dissolved species and transport of

water, hydrogen and oxygen would be useful to better quantify the importance of cross membrane diffusion on both the steady state and the transient performance.

$$j_V = A_{Pt,V} \cdot i_{Pt} + \frac{D_{H_2,mem} \cdot c_{H_2,mem} \cdot 2F}{t_{mem} \Delta x} \quad [27]$$

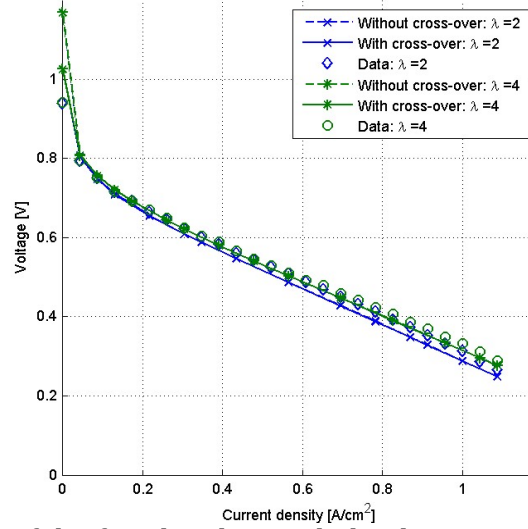


Figure 5. Comparison of the fitted and recorded polarisation curves. The effect of adding a cross over model can be seen in the difference between the dashed and the solid lines.

Fitted Parameters

The fitted parameter values are given in TABLE III. In order to better assess the ability of the model to estimate electrode parameters, a literature review of HTPEM electrode parameters has been performed. In the following sections, the fitted values are discussed in the light of available literature data.

TABLE III. Fitted model parameters.

Fit	$A_{Pt,m}$	α	$A_{C,m}$	$L_{H_3PO_4}$	C_{dl}	t_{CL}	R_{cell}
Base fit	44.6 m ² g ⁻¹	0.762	279 m ² g ⁻¹	0.518 mg cm ⁻²	109 F m ²	26.1 μm	0.131 Ω cm ⁻²

TABLE IV. ECSA values from various sources.

Source	ECSA [m ² g ⁻¹]	Comments
(29)	45 – 69	PTFE bonded electrodes. Surface area determined by microscopy or by measuring hydrogen adsorption.
(35)	~ 35, ~16, ~14	Electrodes with acid doped PBI as binder. 20%, 40% and 60% Pt/C catalysts. Measured using cyclic voltametry (CV).
(36)	17.2, 7.8	PBI bonded electrodes with 40% Pt/C. Before and after 300 h degradation test. Measured using CV.
(37)	12-24	Measured using CV. Depending on measurement conditions.
(34)	41-51	Measured using CV. Varied with CL PBI content. PBI bonded electrodes with 2/3 Pt/C catalyst.

Catalyst surface area. One of the most interesting parameters is the catalyst ECSA. If this value is low, it means that the catalyst is not used efficiently. A range of

measured ECSA values from literature are given in TABLE IV. The value obtained using the model is high compared to most of the sources, but in the lower range of the data from Kunz and Gruver (29). The result is in the range of values obtained by Lobato et al. (34). The tested MEA is similar to the ones tested by Lobato et al in both catalyst composition (60% Pt/C vs. 2/3 Pt/C) and membrane type (Post doped). Thus, the result is deemed realistic.

Transfer coefficient. The transfer coefficient α is of similar importance as the ECSA. It greatly affects the polarisation behaviour and impedance response of the fuel cell. Transfer coefficient values from a number of sources are listed in TABLE V. The fitted value of 0.762 is between the values used in the models by Shamardina et al. (38) and Sousa et al. (8). Out of the experimental studies, the agreement is best with McBreen et al. (39) who obtained $\alpha \approx 0.7$ at 160 °C. It is worthwhile to note that there is a significant disagreement as to the true value of α in PA. This is especially true for the models, but the experimental results also differ. The fact that some observe the transfer coefficient to change with temperature, while others observe it to be constant illustrates the challenges in properly modelling the kinetics of HTPEM fuel cells.

TABLE V. Transfer coefficient values from various modelling and experimental studies.

Reference Type	Transfer coefficient	Sources	Comments
Models	0.2	(18)	
	0.73	(8,40)	
	0.8	(38)	
	0.89	(10)	
	1	(41,42)	
	2	(9,11,43,44)	
Experimental studies	0.56	(45)	T=116 °C ,85% H ₃ PO ₄
	0.61-0.81	(46)	RDE, Temperature dependent (100-251 °C)
	0.63 +/- 0.05	(47)	98% H ₃ PO ₄ ,constant in the range 25-150 °C
	2.3RT/0.12F	(39)	RDE, 89.5% H ₃ PO ₄ , Tafel slope ~120mV / decade up to 175 °C
	1	(29,48)	PTFE bonded electrodes. Various temperatures and concentrations.

Carbon surface area. No information was available on the surface area of the catalyst carbon support. Kim et al.(49) compiled a list of the carbon surface area of various catalyst powders. These areas range from 242 m² g⁻¹ to 1475 m² g⁻¹. In that light, the fitted value of 279 m² g⁻¹ seems reasonable, considering that the binding of the particles and filling of micropores with acid may reduce the effective pore surface area.

CL acid content. The acid content of the catalyst layer is also a matter of some interest. This affects the performance by controlling the conductivity of the CL. In the actual fuel cell, it also affects the ECSA. At higher acid loading, more of the pore surface is covered, adding more catalyst to the triple phase boundary. Due to the assumption of uniform acid distribution, this effect is not accounted for by the model. A few experimental studies have investigated the PA content of HTPEM

catalyst layers. Kwon et al. (50) tested the performance of HTPeM fuel cells with different CL acid doping. The best performance was obtained in the range of 8 to 17 mg cm⁻², which is more than an order of magnitude larger than the fitted value. Another study by Wannek et al. (51) measured changes of acid content of the CL. Three different MEAs with very different initial CL acid loadings of 10 mg cm⁻² or 20 mg cm⁻² exhibited CL acid contents of between 3 mg cm⁻² and 6 mg cm⁻² after operation. While these numbers are closer to the fitted value, there is still a factor of 6 of difference between the lower value and the fit. Some of the difference may be ascribed to the CLs of Wannek et al. being thicker by a factor of 2 or more. Another reason could be the assumptions applied in calculating the CL conductivity of this model. To test this, a small change is made in the conductivity model. Instead of using the conductivity of free PA, equation [12] is used. Here $\epsilon_{PA,PBI}$ is calculated using the local ratio of PA and PBI. It should be noted that the accuracy of the relation is doubtful in this case, since X is even higher in the CL than in the membrane. An illustration of the effect of the CL conductivity on the cell performance is given in Figure 6 and Figure 7.

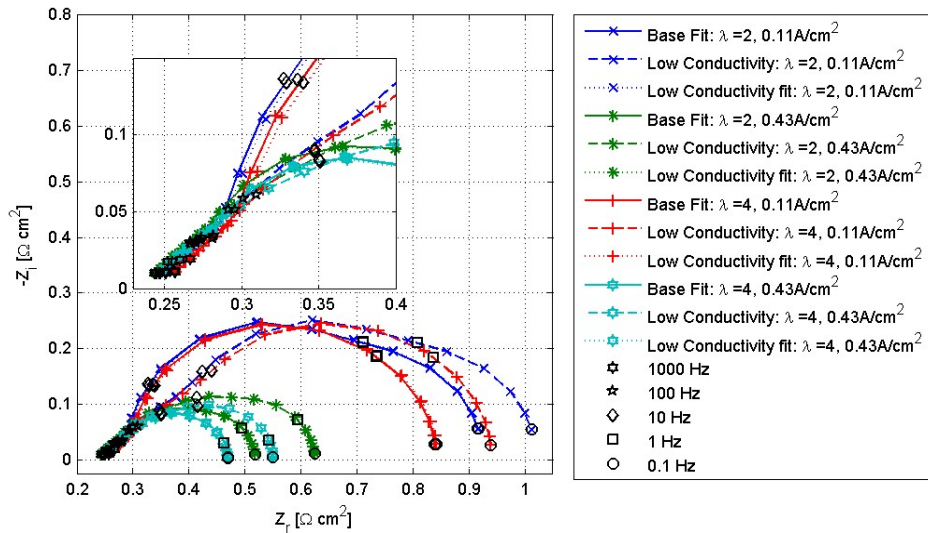


Figure 6. Effect of changing the CL conductivity model. Note the very small difference between the base fit and the low conductivity fit.

The reduced conductivity decreases the voltage of the cell across the operating range as seen in Figure 7 on the left. While the decreased conductivity causes the slope of the polarisation curve to be steeper, the losses are not of purely ohmic in nature, since the impedance spectra are not significantly displaced in the high frequency region. Around 0.7 A cm⁻² the polarisation curves change slopes in a way normally associated with concentration losses. This is interesting, since no parameters relating to reactant transport have been changed. The effect can be observed in the right plot on Figure 7. Here, the lower CL conductivity results in higher overpotentials close to the membrane. This is because the reaction front shifts towards the membrane when the ionic conductivity decreases. Since the O₂ concentration is lower at the membrane, higher overpotentials are needed to sustain the reaction. At higher CL conductivity, the reaction rate is more uniformly distributed in the CL, reducing the overpotential. In order to see the effect on the fitted parameters, the model is fitted with the base fit as start guess. The resulting polarisation curves and impedance spectra are almost coincident with the base fit. The resulting fitting parameters are compared to the base fit in TABLE VI. The main

difference is seen in the PA loading as should be expected. The low conductivity case has 80% higher CL PA content. Since the PA now occupies a larger volume, two additional changes occur: The CL thickness increases, increasing the CL volume to accommodate the extra PA. Also, the carbon surface area is almost halved, reducing the Knudsen diffusion resistance accordingly. The other parameters only vary on the third significant digit. The acid content of the catalyst layer is still low compared to the values reported by Kwon et al. (50) and Wannek et al. (51). An explanation for this may be the mobility of phosphoric acid within the MEA. A recent study by Eberhardt et al. (52) demonstrated that significant amounts of phosphoric acid are transported to the anode GDL and channel at higher current densities. The acid diffused back when the current was lowered, but this process was slower. The results of the parameter fitting may be an indication that the catalyst layers are being drained of PA during operation.

TABLE VI. Fitting parameters for the low membrane conductivity fit.

Fit	$A_{Pt,m}$	α	$A_{C,m}$	$L_{H_3PO_4}$	C_{dl}	t_{CL}	R_{cell}
Base fit	44.6 m ² g ⁻¹	0.762	279 m ² g ⁻¹	0.518 mg cm ⁻²	109 F m ²	26.1 μm	0.131 Ω cm ⁻²
Low conductivity fit	44.9 m ² g ⁻¹	0.761	149 m ² g ⁻¹	0.940 mg cm ⁻²	112 F m ²	27.6 μm	0.130 Ω cm ⁻²

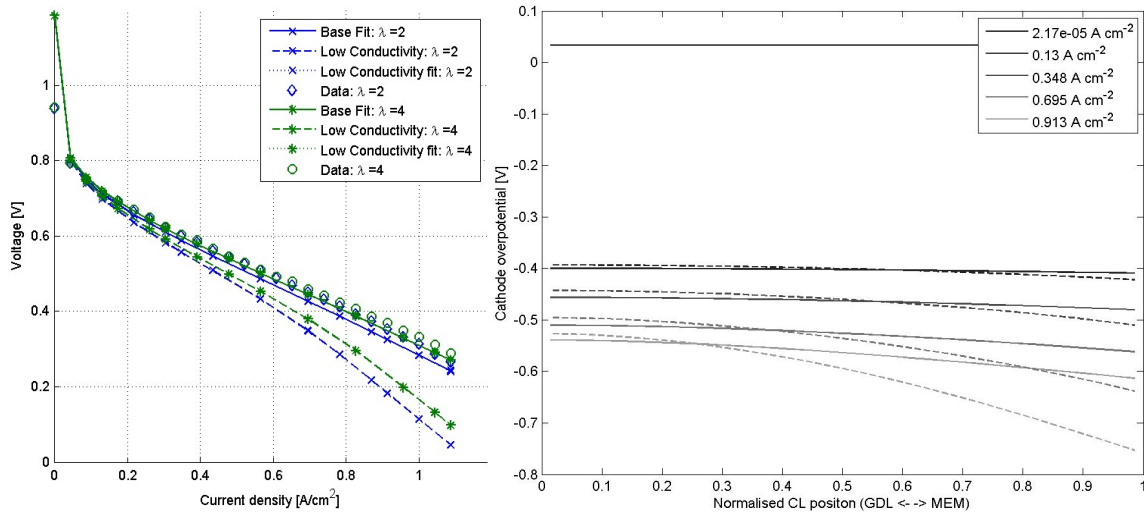


Figure 7. Left: Illustration of the effect of CL conductivity on the polarisation curves. Right: Cathode overpotential at different current densities. Comparison of high (full line) and low (dashed line) CL conductivity using base case parameters.

Double layer capacitance. When normalising the double layer capacitance with respect to the fitted platinum area, we get: $C_{dl,Pt} = C_{dl}/(L_{Pt} \cdot A_{Pt,m}) = 0.154 \text{ F m}_{Pt}^{-2}$. This value is in range of the double layer capacitance on bare metal as tabulated in Orazem and Tribollet (53).

Catalyst layer thickness. The thickness of the catalyst layer is reported by Danish Power Systems to be around 25 μm. Considering the simplifications of the model and the uncertainties and variations in catalyst layer thickness, the fitted value of 26.1 μm is a reasonable estimate.

Contact Resistance. The fitted contact resistance contributes more than half of the total cell resistance. A study by Diedrichs et al. (54) using a MEA from DPS showed that the total cell resistance, using a serpentine flow field, decreased with compression from $0.25 \Omega\text{cm}^2$ at 0.5 MPa to about $0.1 \Omega\text{cm}^2$ at 5 MPa. Thus, it is plausible that there is a significant contribution from poor contact in the cell assembly in the present case. It should, however be borne in mind that the model assumes constant acid content in the membrane. This assumption is not valid if significant acid migration takes place. In case of significant acid migration, the contact resistance is likely overpredicted, while the membrane resistance is underpredicted. Distinguishing these two contributions is not possible with the current setup. In the future, it would be advantageous to measure the voltage directly on the flow plate to minimise the contribution from contact resistance.

Gas dynamics analysis

The attribution of the individual parts of fuel cell impedance spectra is a matter of some controversy. The low frequency loop is alternately interpreted as a result of diffusion impedance (55,56) and as a result of concentration oscillations in the flow channel (16,57–59). This section is devoted to an investigation of this phenomenon. The plots of Figure 8 show simulated spectra for three different situations: One using the full dynamic model, one where the gas composition in the channel is fixed at the steady state value, and one where the gas composition in the entire electrode is fixed. When fixing the gas channel composition, the whole of the low frequency loop disappears. This happens at both low and high current. This strongly indicates that the usual practice of modelling the low frequency loop using a bounded Warburg impedance is not accurate, since the distinct low frequency loop derives from the channel dynamics. A similar conclusion was reached in a recent paper by Kulikovsky and Shamardina (60) using an analytical model for the transient behaviour of the flow channel.

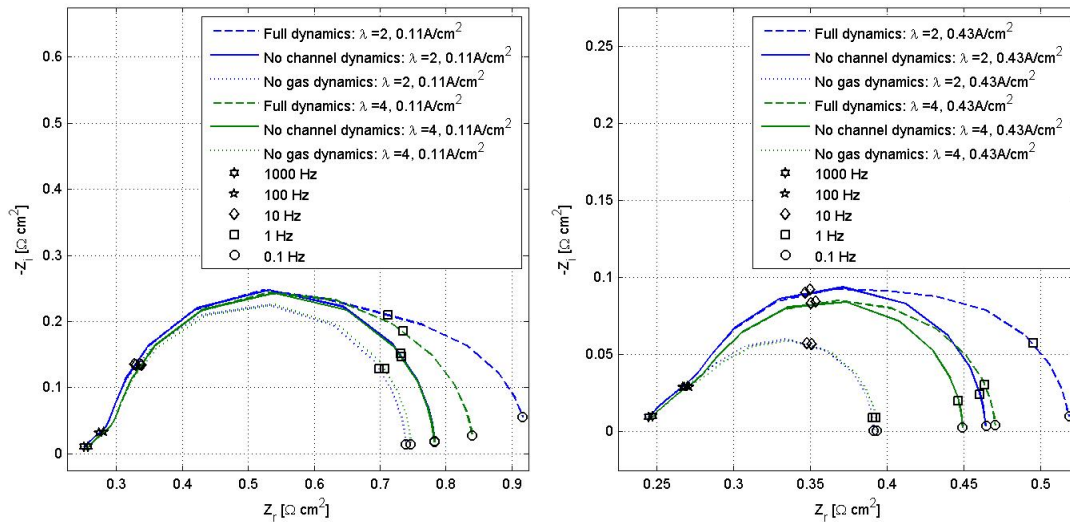


Figure 8. Comparison of simulated impedance spectra with different levels of gas dynamics enabled.

The diffusion inside the porous media does play a role in the impedance, however. The importance of the diffusive contribution is higher at higher current. At 0.11 A cm^{-2} , the spectra with constant channel composition are almost coincident, while at 0.43 A cm^{-2} , the impedance is significantly larger at low stoichiometry. When fixing the total gas composition, the spectra shrink once more compared to the case of constant channel composition only. This effect is most prominent at 0.43 A cm^{-2} and $\lambda = 2$. When the whole gas composition is fixed, the spectra are coincident both at low and high current. At high current, the top point of the intermediate frequency loop moves towards higher frequency, indicating that the time constants of diffusion are indeed slower than those of the electrode kinetics, but not enough for the resulting loops to be distinguishable in the impedance spectra.

Conclusions

In this paper, an HTPEM fuel cell model capable of simulating both impedance spectra and polarisation curves has been developed. The model is capable of producing acceptable simultaneous fits to two polarisation curves recorded at different stoichiometries and four impedance spectra recorded at different stoichiometries and/or currents. The main purpose of the model is to estimate unknown fuel cell parameters. The estimated parameters are all within range of values found in the literature, except for the catalyst layer acid content, which is significantly lower than literature values. The discrepancy may be explained by phosphoric acid migration during operation. The model also provides a means of analysing individual contributions to the impedance spectra. The effects of gas dynamics were investigated. The dynamics of the channel account for the low frequency loop, while the dynamics of the porous media contribute to the intermediate frequency loop. This suggests that the standard approach of representing the low frequency loop by a bounded Warburg impedance is incorrect. Future work on this model could include properly accounting for crossover of reactants and water to mitigate the overprediction of the voltage at open circuit. A possible application of the model could be in analysis of degradation in long term tests.

Acknowledgement

The authors would like to thank the Danish Energy Technology Development and Demonstration Programme (EUDP) for funding this work through the Supplemental Power Generation project. Dr. Anders Christian Olesen is acknowledged for contributing with insight into how to properly model the electrochemical reactions.

References

1. S. K. Das, A. Reis, and K. J. J. Berry, *J. Power Sources*, **193**, 691–698 (2009).
2. A. D. Modestov, M. R. Tarasevich, V. Y. Filimonov, and E. S. Davydova, *Electrochim. Acta*, **55**, 6073–6080 (2010).

3. C.-H. Wan and Q.-H. Zhuang, *Electrochim. Acta*, **52**, 4111–4123 (2007).
4. J. E. Hu, Z. Liu, B. W. Eichhorn, and G. S. Jackson, *Int. J. Hydrogen Energy*, **37**, 11268–11275 (2012).
5. Q. Li, J. O. Jensen, R. F. Savinell, and N. J. Bjerrum, *Prog. Polym. Sci.*, **34**, 449–477 (2009).
6. A. R. Korsgaard, R. Refshauge, M. P. Nielsen, M. Bang, and S. K. Kær, *J. Power Sources*, **162**, 239–245 (2006).
7. K. Scott, S. Pilditch, and M. Mamlouk, *J. Appl. Electrochem.*, **37**, 1245–1259 (2007).
8. T. Sousa, M. Mamlouk, and K. Scott, *Chem. Eng. Sci.*, **65**, 2513–2530 (2010).
9. K. Jiao and X. Li, *Fuel Cells*, **10**, 351–362 (2010).
10. C. Siegel, G. Bandlamudi, and A. Heinzl, *J. Power Sources*, **196**, 2735–2749 (2011).
11. D. F. Cheddie and N. D. H. Munroe, *J. Power Sources*, **160**, 215–223 (2006).
12. P. Moçotéguy, B. Ludwig, J. Scholta, R. Barrera, and S. Ginocchio, *Fuel Cells*, **9**, 325–348 (2009).
13. J. L. Jespersen, E. Schaltz, and S. K. Kær, *J. Power Sources*, **191**, 289–296 (2009).
14. S. Galbiati, A. Baricci, A. Casalegno, and R. Marchesi, *Int. J. Hydrogen Energy*, **38**, 6469–6480 (2013).
15. Y. Bultel, L. Génies, O. Antoine, P. Ozil, and R. Durand, *J. Electroanal. Chem.*, **527**, 143–155 (2002).
16. G. Maranzana et al., *Electrochim. Acta*, **83**, 13–27 (2012).
17. S. K. Roy, M. E. Orazem, and B. Tribollet, *J. Electrochem. Soc.*, **154**, B1378–B1388 (2007).
18. M. Boaventura, J. M. Sousa, and A. M. Mendes, *Int. J. Hydrogen Energy*, **36**, 9842–9854 (2011).
19. O. Shamardina, M. S. Kondratenko, A. V. Chertovich, and A. A. Kulikovskiy, *Int. J. Hydrogen Energy*, **39**, 2224–2235 (2014).
20. Y. Shi, H. Wang, and N. Cai, *J. Power Sources*, **208**, 24–34 (2012).
21. A. Baricci, M. Zago, and A. Casalegno, *Fuel Cells*, **14**, 926–937 (2014).
22. J. R. Vang, S. J. Andreasen, and S. K. Kær, *J. Fuel Cell Sci. Technol.*, **9**, 021005–1 – 021005–9 (2012).
23. D. MacDonald and J. Boyack, *J. Chem. Eng. Data*, **14**, 380–384 (1969).
24. K. Klinedinst, J. A. S. Bett, J. Macdonald, and P. Stonehart, *Electroanal. Chem. Interfacial Electrochem.*, **57**, 281–289 (1974).
25. K. E. Gubbins and R. D. Walker, *SOLUBILITY AND DIFFUSIVITY OF HYDROCARBONS AND OXYGEN IN FUEL CELL ELECTROLYTES*, p. 68, Gainesville, Florida, (1965).
26. D. Tromans, *Hydrometallurgy*, **48**, 327–342 (1998).
27. A. L. Magalhães, P. F. Lito, F. A. Da Silva, and C. M. Silva, *J. Supercrit. Fluids*, **76**, 94–114 (2013).
28. Y. Ma, thesis, CASE WESTERN RESERVE UNIVERSITY (2004).
29. H. R. Kunz and G. A. Gruver, *Electrochim. Acta*, **23**, 219–222 (1978).
30. R. B. Bird, W. E. Steward, and E. N. Lightfoot, *Transport Phenomena* P. K. Wayne Anderson, Editor, Revised 2n., John Wiley & Sons, Inc., (2007).
31. N. . Zamel, X. . Li, and J. . Shen, *Energy and Fuels*, **23**, 6070–6078 (2009).
32. ISO, 12 (2013).
33. Freudenberg FCCT SE & CO. KG, 1–2 (2013).
34. J. Lobato, P. Cañizares, M. A. Rodrigo, J. J. Linares, and F. J. Pinar, *Int. J. Hydrogen Energy*, **35**, 1347–1355 (2010).

35. M. Mamlouk and K. Scott, *Proc. Inst. Mech. Eng. Part A J. Power Energy*, **225**, 161–174 (2011).
36. Y. Zhai, H. Zhang, D. Xing, and Z.-G. Shao, *J. Power Sources*, **164**, 126–133 (2007).
37. K. Kwon, J. O. Park, D. Y. Yoo, and J. S. Yi, *Electrochim. Acta*, **54**, 6570–6575 (2009).
38. O. Shamardina, A. Chertovich, A. A. Kulikovsky, and A. R. Khokhlov, *Int. J. Hydrogen Energy*, **35**, 9954–9962 (2010).
39. J. Mccreen, W. E. O. Grady, and R. Richter, *J. Electrochem. Soc.*, 1215–1216 (1984).
40. M. Mamlouk, thesis, University of Newcastle upon Tyne (2008).
41. J. Peng and S. J. Lee, *J. Power Sources*, **162**, 1182–1191 (2006).
42. J. Peng, J. Y. Y. Shin, T. W. W. Song, and E. Ubong, *J. Power Sources*, **179**, 220–231 (2008).
43. D. F. Cheddie and N. D. H. Munroe, *Int. J. Hydrogen Energy*, **32**, 832–841 (2007).
44. K. Jiao, I. E. Alaefour, and X. Li, *Fuel*, **90**, 568–582 (2011).
45. A. J. Appleby, *J. Electroanal. Chem. Interfacial Electrochem.*, **24**, 97–117 (1970).
46. S. J. Clouser, J. C. Huang, and E. Yeager, *J. Appl. Electrochem.*, **23**, 597–605 (1993).
47. B. R. Scharifker, P. Zelenay, and J. O. M. Bockris, *J. Electrochem. Soc.*, **134**, 2714–2725 (1987).
48. H. R. Kunz and G. A. Gruver, *J. Electrochem. Soc.*, **122**, 1279–1287 (1975).
49. M. Kim, J.-N. Park, H. Kim, S. Song, and W.-H. Lee, *J. Power Sources*, **163**, 93–97 (2006).
50. K. Kwon, T. Y. Kim, D. Y. Yoo, S.-G. Hong, and J. O. Park, *J. Power Sources*, **188**, 463–467 (2009).
51. C. Wannek, I. Konradi, J. Mergel, and W. Lehnert, *Int. J. Hydrogen Energy*, **34**, 9479–9485 (2009).
52. S. H. Eberhardt et al., *J. Electrochem. Soc.*, **162**, F310–F316 (2015).
53. M. E. Orazem and B. Tribollet, *Electrochemical Impedance Spectroscopy* I. John Wiley & Sons, Editor, John Wiley & Sons, Inc., (2008).
54. A. Diedrichs, M. Rastedt, F. J. Pinar, and P. Wagner, *J. Appl. Electrochem.*, **43**, 1079–1099 (2013).
55. T. E. Springer, T. A. Zawodzinski, M. S. Wilson, and S. Gottesfeld, *J. Electrochem. Soc.*, **143**, 587–599 (1996).
56. M. Mamlouk and K. Scott, *Electrochim. Acta*, **56**, 5493–5512 (2011).
57. I. A. Schneider, S. A. Freunberger, D. Kramer, A. Wokaun, and G. G. Scherer, *J. Electrochem. Soc.*, **154**, B383–B388 (2007).
58. I. A. Schneider, D. Kramer, A. Wokaun, and G. G. Scherer, *J. Electrochem. Soc.*, **154**, B770 (2007).
59. J. Mainka, G. Maranzana, J. Dillet, S. Didierjean, and O. Lottin, *J. Electrochem. Soc.*, **157**, B1561–B1568 (2010).
60. A. Kulikovsky and O. Shamardina, *J. Electrochem. Soc.*, **162**, F1068–F1077 (2015).
61. D.-T. Chin and H. Chang, *J. Appl. Electrochem.*, **19**, 95–99 (1989).
62. M. Bang, thesis, Aalborg University (2004).

Appendix

The molal solubility of O₂ in water ($b_{O_2,water}$) as a function of temperature is calculated using equation 18 in the work by Tromans (26). The molal solubility is converted to molar solubility:

$$c_{0,O_2,water} = \frac{b_{O_2,water} \cdot \rho_{sat,water}}{1 + b_{O_2,water} \cdot M_{O_2}} \quad [28]$$

Here $\rho_{sat,water}$ is the density of saturated liquid water at the relevant temperature.

The viscosity of PA is fitted to data tabulated by Chin and Chang (61). The fit was obtained using the Matlab® Curve fitting toolbox. The relation is given below.

$$\mu_{PA} = (2.7007 + 37.605 y_{P_2O_5}) \exp\left(\frac{14.626 + 1050.4 y_{P_2O_5}}{T - 273.15}\right) \cdot 10^{-4} \quad [29]$$

TABLE VII. PA concentration fit coefficients

Coefficient	Value
w_1	0.7856
w_2	0.0002786
w_3	-0.01944
w_4	0.669
w_5	-0.4927

TABLE VIII. Coefficients for the solubility and diffusivity of O2 in PA.

Coefficient number (i)	Solubility (c _i)	Diffusivity (d _i)
1	$4.11500117966429 \cdot 10^{-5}$	0.654661162430493
2	0.296030815669062	6.72763244794933
3	3.23663842302862	-

TABLE IX. Reference values for binary diffusivities.⁶²

Gas pair	D_{ij} [m ² s ⁻¹]	T_0 [K]	γ
O ₂ – N ₂	$2.02 \cdot 10^{-5}$	293.15	1.728
O ₂ – H ₂ O	$2.44 \cdot 10^{-5}$	293.15	1.967
H ₂ O – N ₂	$2.43 \cdot 10^{-5}$	293.15	2.073